In situ DRIFT, Raman, and XRF implementation in a multianalytical methodology to diagnose the impact suffered by built heritage in urban atmospheres

Olivia Gómez-Laserna[1] · Iker Arrizabalaga[1] · Nagore Prieto-Taboada[1] ·
María Ángeles Olazabal[1] · Gorka Arana[1] · Juan Manuel Madariaga[1]

Abstract This work addresses the evaluation of an innovative mutianalytical method to assess the conservation state of a fifteenth century palace house. With the goal of reducing the handicaps of field analysis, the in situ spectroscopic assessment, often based on the use of X-ray fluorescence and Raman spectrometers, was complemented by the use of diffuse reflectance infrared Fourier transform spectroscopy. In this manner, its usefulness as a diagnostic tool to discover the origin and mechanisms of the damage caused by atmospheric and infiltration water attacks were thoroughly examined. Moreover, the study was extended in the laboratory to increase the information obtained by nondestructive techniques. The results revealed a severe material loss caused by soluble salts. Thus, a noninvasive sampling method using cellulose patches was tested to study the amount and mobility of salts by means of ion chromatography. Finally, to establish the chemical degradation processes that are occurring in the palace, a chemometric analysis of the quantitative data as well as the construction of thermodynamic models was done to advise on the required restorative actions.

Keywords X-ray fluorescence · Raman spectroscopy · Diffuse reflectance infrared Fourier transform · Soluble salts · Chemometric · Thermodynamic modeling

✉ Olivia Gómez-Laserna
olivia.gomez@ehu.eus

[1] Department of Analytical Chemistry, University of the Basque Country (UPV/EHU), P.O. Box 644, 48080 Bilbao, Spain

Introduction

A few years ago, the study of the conservation state of our built heritage required the collection of samples to perform analyses in the laboratory. However, the development of portable devices allows us to perform these studies in situ with successful results. In fact, the use of nondestructive portable techniques is growing over the use of traditional methods, and many methods based on the use of spectroscopic devices have been developed. In this sense, the advantages of in situ spectroscopic assessment based on Raman spectroscopy and the added benefits of its combination with different analytical methods to study the degradation causes of a wide variety of building materials have been highlighted recently [1–4]. Unfortunately, its application as the main technique in this field has some drawbacks, which could be minimized to increase the information obtained in situ.

The main disadvantages [4–6] are related to the composition of built heritage materials since they often contain chromophores that can produce great fluorescence in Raman spectroscopy, hampering the in situ analysis. Some of them are inherent to the compounds present in the materials, such as clays [4, 7, 8]. By contrast, others are incorporated in the material by infiltration or deposition of external agents as organic matter or dust [9]. Although some strategies such as photobleaching (overexposure to a laser) can help to reduce their effect, the reality is that the methods that could be use in field analyses are complex to accomplish. Adding to this issue, the interferences arising from the environmental conditions [4, 6, 10], such as the effect of strong sunlight, sometimes make the analysis more complicated, and this could result in the overlapping of peaks or even, in the worst cases, in the absence of a valid signal. For these reasons, to reduce the handicaps presented, other techniques should be considered as complementary tools for molecular characterization analysis.

In this regard, Fourier transform infrared spectroscopy (FTIR) seems to be a powerful technique to study compounds of different nature since it has great flexibility, as it can be used in various modes, such as diffuse reflectance, specular reflectance, and attenuated total reflection [11–14]. Besides, according to the literature, different kinds of analyses have been done in several materials, such as pigments, binders, marbles, and limestones [15–18].

Focusing on the in situ measurements performed in reflectance mode, we highlight two types of reflectance equipment; fiber-optic reflectance spectroscopy (FORS) and handheld FTIR spectroscopy devices. The first one has been applied to a variety of samples, achieving very good results [1, 18–20]. Nevertheless, in recent work [21, 22] the benefits and limitations of non-FORS equipment with regard to built heritage have been discussed, opening a new path in in situ analyses by reflectance spectroscopy.

In this way, the use of diffuse and specular reflectance allows us to perform analyses in solid materials without sampling or sample preparation. However, the spectra obtained by means of diffuse, specular, or total reflectance may be difficult to interpret, as their quality heavily depends on the characteristics of the sample surface. In the measurements performed in situ by reflectance spectroscopy, the biggest drawback is that the diffuse component cannot be optically separated from the specular one, and this interaction is the main source of distortions. Hence, in the in situ spectra obtained, there are usually inverted bands created by the Reststrahlen effect [23], and thus the interpretation of these spectra can be difficult.

Nevertheless, recently published work [22–24] has tested the possible application of diffuse reflectance infrared Fourier transform (DRIFT) spectroscopy to perform in situ analysis of building materials, studying successfully how to reduce the spectral distortions by applying mathematical algorithms as well as indicating a few guidelines to acquire good in situ spectra.

For the purpose of reducing the handicaps of field analysis, we evaluate a novel multianalytical method to diagnose the state of conservation of a historical palace house. To achieve this goal, the in situ spectroscopic assessment often based on the use of X-ray fluorescence (XRF) and Raman spectrometers was complemented by the use of DRIFT spectroscopy, studying in this work its usefulness as a diagnostic tool to find out the origin, mechanisms, and severity of the damage suffered by the building materials. Then, to corroborate and increase the information obtained in situ, the study was extended by the use of nondestructive techniques in the laboratory.

In addition, because one of the main dangerous types of damage in the study of monumental stone decay is related to the effect of soluble salts [4, 25], their quantification by a noninvasive sampling method is advised to complete the spectroscopic assessment. Lately, several studies have reported [26] that use of agar-based gels is an interesting method to sample black crusts and that they are a useful tool in the risk assessment analysis of built heritage affected by atmospheric pollution. Nonetheless, their penetration capacity is not the most suitable for monitoring the soluble salt content. Therefore, in this work, the utility of a noninvasive method based on paper pulp poultices [27] was tested for the extraction of soluble salt samples. In this manner, the amount and mobility could be studied in depth using salt distribution models based on the quantitative results obtained by ion chromatography.

Finally, to corroborate and establish the manner in which the salts cause damage, a multivariate analysis of the data was performed, and thermodynamic models of the different degradation processes that are occurring in the palace were constructed, and the findings are thoroughly discussed.

Materials and methods

Location and description of the palace house

Guevara Palace is located in the village of Segura (Gipuzkoa, Basque Country, northern Spain) (Fig. S1), along the Oria river, on ground mostly composed of limonites and sandstones. According to the lithology [28] of the area, the soils are rich in organic matter, and have a high content of silt and clay, which increases the cation-exchange capacity ($Ca^{2+} > Mg^{2+} > K^+$) of the soil. Furthermore, given its composition and the oceanic climate of the area, the high rainfall could increase the percolation of alkalizing elements, thereby leading to acid saturation of the soil.

On the other hand, the main economic activities of the village are related to the livestock and meat processing industry, although nonferrous metal and paper industries are also located in nearby areas. Nevertheless, reports of the chemical quality of air and water show admissible levels [29].

This building is one of the best examples of a Gothic pre-Renaissance urban palace in the Basque Country. This palace from the fifteenth century is classified as a cultural asset (7/90, Basque Cultural Heritage Law), having been declared a national historic monument (Decree Number 265/1984). Regrettably, the characteristic components of this construction system are in danger of disappearing, as most of the interventions done are limited to maintaining the facade, losing a large part of the building elements of great historical value.

The building has undergone several transformations, and the areas adjacent to the central body are today used as housing. The rehabilitation work, which is currently in progress, is focused on refurbishing the central building, preserving unchanged the facade and central inner wall, known as the firewall, typical of the time.

The front elevation of the building has two floors, with the main body having architectural forms such as a balls cornice and gargoyles. The main and back entrances are composed of

arches, giving direct access to the ground floor (under restoration) and the hall, where the access ladders to the upper floor (fully restored) are found. Besides, to join both rooms, one more arch, which has an important structural function and historical value, can be found in the central inner wall.

The building is constructed from sandstone ashlars over a concrete base. However, in the interior of the building, the blocks are visible only in the central wall, as the rest of them have been leveled and plastered (Fig. 1f). Moreover, the joint mortar of the facade is practically absent, and the interior mortar is apparently composed of cement and sand.

Sampling

The visual inspection allowed us to identify the different types of damage (Fig. 1). In this way, several black crusts were observed in the main facade, being especially notable in the coat of arms and in the basal voussoirs of the entrance arch. Moreover, the latter suffers from material loss, showing intense disaggregation in decorative ornaments. Besides, areas of different colors, flaking, and efflorescences were heterogeneously distributed along the surface of the facade. Finally, ferns, mosses, and lichens were growing on the gargoyles and in the areas near the drainpipe of the roof gutter.

In addition, inside the building, given its cultural value and its structural function, the arch of the central wall was studied. Several salt crusts (approximate thickness of 3 mm) were observed on the joint mortars and sandstone. Moreover, the base of the arch was wet to the touch and showed severe degradation.

After indentifying the points of interest, we performed a first in situ investigation during May, after some days without rain. More than 100 in situ spectroscopic measurements were collected. Besides, measurements of temperature and relative humidity were taken outside as well as inside the building (21 °C and 65 % and 19 °C and 71 %, respectively) to help establish the chemical degradation mechanisms.

As a result of this screening, in November, a second investigation was conducted, in which over 120 in situ spectroscopic measurements were performed in the nonrestored areas (external 9 °C and 73 %, internal 10 °C and 77 %). On this occasion, although some efflorescences were observed in the arch of the inner wall, the salt crust measured previously had almost disappeared, probably as a consequence of the change in climatic conditions.

After the in situ assessment, a very small amount (approximately 0.10 g) of nondegraded sandstone was collected to complement the information about its original composition in the laboratory. Also, some samples were collected from the facade using a chisel (between 0.10 and 0.15 g for each one) to continue the spectroscopic study. Moreover, according to the salt distribution detected in situ in the historical arch, samples with potentially soluble content (from zones P1–P7) (Table 1) were extracted for quantitative analysis using cellulose patches since destructive sampling was restricted inside the palace.

The extraction method is based on the suggestion of Arnold and Zehnder [30], who state that salt content is seldom homogeneous throughout a wall. Eight samples were taken by cellulose patches approximately 12 cm^2 in area and 5 mm thick soaked in deionized water with a pulp-to-water weight ratio of about 1:8. They were applied to the sampling points for 2 h [27], and then they were removed.

Fig. 1 Selected photographs of the deterioration observed in Guevara Palace. **a** Different colorations and material loss found in the basal voussoir of the entrance arch. **b** Black crust and efflorescences over the coat of arms. **c** Reddish areas. **d** Disaggregations and efflorescences of the sandstone ashlars. **e** In situ X-ray fluorescence analysis of blackened areas. **f** In situ diffuse reflectance infrared Fourier transform (DRIFT) analysis of the inner arch

Table 1 Classification of the zones analyzed spectroscopically in the inner arch

	P1	P2	P3	P4	P5	P6	P7	P8
Height (m)	0	0.2	0.4	0.6	0.8	1.2	1.6	2

Instruments and methods

In situ equipment

To perform the in situ analysis, three portable instruments were used directly on different materials of the facade. In this way, to determine the elemental composition of the original materials, a semiquantitative in situ analysis was performed using a portable XRF spectrometer (X-MET5100 model, Oxford Instruments, UK). The equipment has a focus spot diameter of 10 mm and a rhodium X-ray tube that provides a voltage of 40 kV. The calibration was performed with the method of fundamental parameters for different types of materials (nonstandard calibration).

The molecular composition of the samples was determined by a handheld Raman spectrometer (InnoRam, BWSpec, Newark, DE, USA) for both in situ and laboratory measurements. The spectrometer works with a 785-nm laser of variable power to control thermal decomposition. Thanks to the probe, performing microscopic analysis using optical lenses (×4, ×20, and ×50) is also possible, allowing one to measure areas of diameters between 10 and 200 μm. A calibration was done daily using a silicon chip. Spectra were collected in a fixed spectral range from to 175 to 3,000 cm^{-1} with a resolution of 3.5 cm^{-1}, using integration times from 1 to 10 s and 5–35 accumulations to improve the signal-to-noise ratio. Data acquisition was performed with BWSpec version 3.26 (BWSpec, Newark, DE, USA).

In situ diffuse reflectance spectra were acquired with a handheld FTIR spectrometer (4100 Exoscan; Agilent, Santa Clara, CA, USA) with a diffuse reflectance sampling interface with a 10-mm spot diameter, short acquisition times, and 32 accumulations. The Michelson interferometer has a maximum resolution of 4 cm^{-1} and a maximum spectral range of 600–4,000 cm^{-1}. The background is acquired with a diffuse gold reference cap.

All the in situ spectra were processed with Omnic version 7.2 (Thermo Nicolet, Madison, WI, USA), and their interpretation was done using the e-VISART, e-VISARCH, and e-VISNICH spectra databases as well as RRUFF [31–34].

Laboratory equipment

To corroborate the in situ results, a Jasco 6300 FTIR spectrophotometer was used, equipped with a diffuse reflection attachment (DR PR0410M; Jasco, Easton, MD, USA). The spectra obtained were collected in the mid-infrared region (from 400 to 4,000 cm^{-1}), with 32 scans being recorded per spectrum at a spectral resolution of 4 cm^{-1}. The system has a Ge/KBr beam splitter and a deuterated and L-alanine-doped triglycine sulfate detector. All samples were dispersed in a diluent (KBr, 99 %; Sigma Aldrich, USA) at proportions between 5 and 10 % depending on the compound.

To characterize the type of stone, X-ray diffraction analysis of the ground sample was performed with a powder diffractometer (Xpert PRO; PANalytical Ankara, Turkey), equipped with a copper tube ($\lambda Cu_{K\alpha\ mean}$=1.5418 Å, $\lambda Cu_{K\alpha1}$=1.5406 Å, $\lambda Cu_{K\alpha\ 2}$=1.54439 Å), a vertical goniometer (Bragg–Brentano geometry), a secondary graphite monochromator, and a PixCel detector. The measurement conditions were 40 kV and 40 mA, with an angular range scanned between 5° and 70°. For the data treatment and the identification of the mineral present, the software X'pert HighScore (PANalytical, Ankara, Turkey) in combination with the powder diffraction file (PDF-2) database (International Centre for Diffraction Data, Newtown Square, PA, USA) was used.

Finally, to extract the soluble salt content of the cellulose patches, an ultrasound-assisted extraction method [35] was used as an effective alternative to standard EN 16455/2014. In this way, the patches were treated in an ultrasonic bath for 120 min using 100 mL of deionized water. The quantification was done by suppressed ion chromatography using a Dionex ICS 2500 system and an ED50 conductivity detector. For anions, an IonPac AS23 column (4 mm×250 mm) and an IonPac AG23 precolumn (4 mm×50 mm) were used, and as the mobile phase, a solution of 4.5 mM Na_2CO_3 and 0.8 mM $NaHCO_3$ was selected. The suppression current and flow rate applied were 25 mA and 1 mL min^{-1}, respectively. The analysis of cations was conducted using an IonPac CS12A column (4 mm×250 mm) and an IonPac CG-12A precolumn (4 mm×50 mm) from Vertex. As the mobile phase, a solution of 20 mM CH_4SO_3 was used. The suppression current and the flow rate applied were 50 mA and 1 mL min^{-1}. The data processing was performed by means of the program Chromaleon, version 6.60-SP1a (Dionex, Sunnyvale, CA, USA).

To identify correlations between quantified cations and anions, a chemometric model produced by The Unscrambler® version 9.2 (CAMO Sofware, Oslo, Norway) was used. For this purpose, the quantitative data were introduced in units of equivalents to take into account the charge of each ion.

Furthermore, to explain the most relevant decay mechanisms, thermodynamic models were assessed using chemical equilibrium diagrams and information on stability constants included in the free academic programs HYDRA and Medusa, version 15 (Royal Institute of Technology, Stockholm, Sweden) [36].

Results and discussion

In situ results

X-ray fluorescence

In the characterization of the original materials, the analysis of sandstones showed silicon as the main major element, followed by calcium, potassium, and aluminum in a lower proportion. Furthermore, chlorine, sulfur, and iron were identified as minor elements. The remaining composition could correspond to light elements such as sodium and oxygen, but their signals were too low to be detected by the portable equipment.

Given the appearance of the stone and its composition, the main cement could be of micaceous nature [37, 38], although the sandstones that are more yellowish could also contain ferruginous cement. This hypothesis appears consistent with the stone from nearby quarries such as those at Aizpea and Bergara.

In the case of mortars, calcium was identified as the major element, followed by silicon and aluminum in a much lower proportion. The undetected remaining composition could correspond to light elements, mainly sodium and oxygen for this kind of matrix. Thus, it could be classified as sand mortar, corroborating the visual inspection.

Additionally, XRF analyses were performed in approximately the same locations as the Raman and DRIFT measurements, thus contributing to facilitation of the interpretation of the spectra collected.

Finally, despite the appearance of the facade, no signals corresponding to toxic metal pollutants such as copper, zinc, manganese, or lead were identified at a significant level either in degraded areas or in fresh areas. In this sense, destructive analysis to detect heavy pollutants related to traffic or industrial activities was not considered necessary.

DRIFT and Raman spectroscopy

To achieve a correct interpretation of the in situ spectra collected, it is necessary to take into account some concepts related to the distortions observed in the reflectance measurements.

As already mentioned, the biggest drawback of the DRIFT in situ analysis is the appearance of inverted bands in the spectra (Figs. 2a and 3). This effect known as the Reststrahlen effect is very common in most inorganic salts owing to the influence of their absorption index in the specular reflectance measurement [22, 24, 39]. As will be seen, the oxyanion content of samples such as carbonates, sulfates, and silicates causes a great increase of the reflectance, and as a consequence, the inverted bands appear in the corresponding area [23], making the interpretation of the spectra difficult.

However, in the diffuse reflectance measurements, the width of the sample appears larger than in the transmittance measurements as many reflections occur in the sample. Therefore, the intensities of overtones and combination bands increase, helping us to perform correct assignment of the spectra obtained. Moreover, correction algorithms such as the Kramers–Kronig algorithm can be used to attempt to minimize the distortions, although successful results depend on the characteristics of the sample surface [22, 24].

Hence, knowing that the in situ measurements are determined by the properties of the sample and given that, in this case, the surface is not the most suitable for using the correction algorithm of Kramers and Kronig, we performed the spectral assignment on the basis of the secondary bands as well as on he basis of the intensification of the overtones, according to the requirements of each case.

In this way, in relation to the *original composition* of the sandstone, the spectra of several compounds (Table 2) were collected. However, the DRIFT spectra obtained were distorted by the Reststrahlen effect (Fig. 2a). In this way, the regions around 1,000 cm^{-1} (Si–O asymmetric stretching of silicates) and 1,400–1,500 cm^{-1} (the CO_3^{2-} asymmetric stretching) were inverted, and it was not possible to perform the assignment using the main bands. Therefore, the secondary bands and overtones were used. In this way, potassium carbonate (K_2CO_3) was detected by its bands at 2,482, 2,422, and 1,748 cm^{-1}, calcite ($CaCO_3$) was detected by its bands at 2,869, 2,513, and 1,794 cm^{-1}, and a great amount of silicates was detected by the characteristic bands at around 1,000 cm^{-1} and 3,500–3,600 cm^{-1}.

In addition, Raman analysis determined α-quartz (α-SiO_2; detected by its main peak at 464 cm^{-1} and its secondary peak at 263 cm^{-1}) as the major compound. Moreover, as minor compounds, calcite (detected by its principal peak at 1,085 cm^{-1}), hematite (α-Fe_2O_3; identified by its bands at 404 and 289 cm^{-1}), rutile (TiO_2; identified by its bands at 446 and 612 cm^{-1}), and phyllosilicates such as kaolinite [$Al_2Si_2O_5(OH)_4$; identified by its characteristic broad bands at 915, 794, and 745 cm^{-1}] and probably some kind of muscovite [$KAl_2(Si_3Al)O_{10}(OH)_2$; identified by its peaks at 749, 408, and 261 cm^{-1}] were found (Fig. 2b). As a consequence of the clay content and the carbon content (identified by the two characteristic bands at 1,600 and 1,325 cm^{-1}) of the matrix, great fluorescence was observed in all the Raman measurements. Hence, the previous XRF and DRIFT measurements performed in the same areas were crucial to achieve the spectral assignment.

In the case of mortars, calcite and α-quartz were found as major original compounds. The DRIFT analysis corroborated the main composition, detecting calcite and several silicates also.
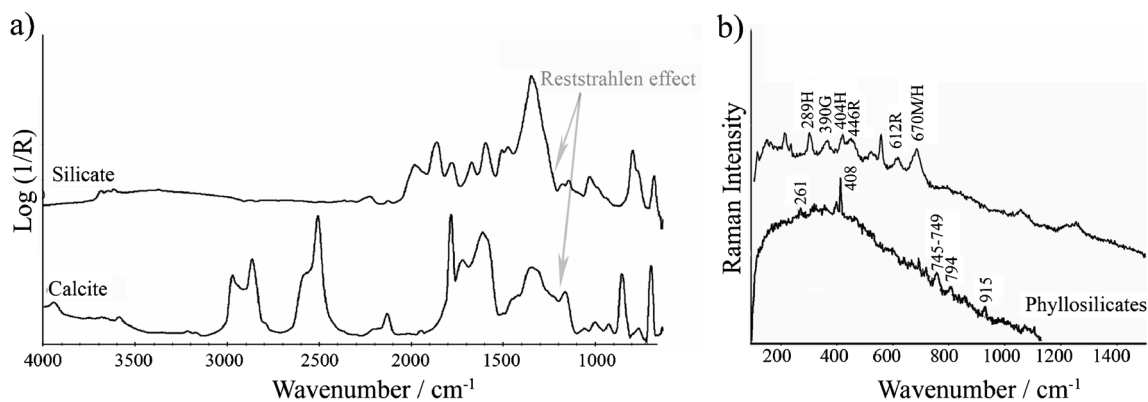
Fig. 2 **a** DRIFT spectra of calcite and silicates identified in situ as original materials of sandstone. **b** Raman spectra of phyllosilicates, hematite (*H*), goethite (*G*), and disordered hematite or magnetite (*M/H*) found in the matrix of sandstone

Once the original nature of each material had been classified, the *degradation compounds* found (Table 2) were classified.

In the analysis of the facade, goethite [α-FeO(OH); detected by its main Raman band at 390 cm^{-1}] (Fig. 2b) and also disordered hematite or magnetite [Fe_3O_4; detected by a broad Raman band at 670 cm^{-1}) were determined as the main degradation compounds of the reddish areas (Fig. 1c). Then, given their location on the facade, they could be transformation products of the original hematite resulting from the action of atmospheric pollutants [40]. The process could start with the formation of crystalline lepidocrocite (γ-FeOOH) and magnetite, which could crystallize and precipitate during the drying stage. In turn, lepidocrocite could be transformed into maghemite (γ-Fe_2O_3) by dehydroxylation and/or into the amorphous ferric oxyhydroxide—$FeO_x(OH)_{3-2x}$—by a dissolution–precipitation process. All these compounds are poorly crystallized and quite unstable. Therefore, they tend to transform into goethite, the most thermodynamically stable mineral phase [41]. Taking into account the nature of iron compounds and their locations, always in yellowish sandstone, we classified this as a direct degradation of the ferruginous cement caused by atmospheric attack. Besides, the dissolution of the cement and the volume changes that occurred during the chemical transformations could produce severe damage such

as disaggregation, fractures, and when the ashlars have structural function, even important loss of stability.

Moreover, in the degraded areas of the facade, calcite, gypsum ($CaSO_4 \cdot 2H_2O$; detected by its main Raman signal at 1008 cm^{-1}), and anhydrite ($CaSO_4$; Raman band at 1,017 cm^{-1}) were found as the main degradation compounds of efflorescences and subefflorescences. Thus, the existence of these compounds, in this form and heterogeneously distributed, suggests the attack of atmospheric pollutants on the original calcite. In this way, carbonic acid and sulfuric acid aerosols [42] can cause the dissolution of the original material and its crystallization into the pores. As a consequence of these dissolution–precipitation and hydration–dehydration processes, severe damage to decorative door elements, flaking, and loss of material could be observed (Fig. 1).

On the other hand, in the areas affected by black crusts, carbon (identified by two broad bands at 1,600 and 1,325 cm^{-1}), calcite, gypsum, and nitromagnesite [$Mg(NO_3)_2 \cdot 6H_2O$; detected by the presence of its main peak at 1,059 cm^{-1}] were observed as degradation compounds by Raman spectroscopy. Moreover, thanks to the DRIFT analysis, the presence of these compounds was corroborated in situ (Fig. 3a). These degradation compounds are usually related to this damage as the crust could act as a catalytic support to promote the oxidation of atmospheric SO_x and NO_x gases [43].
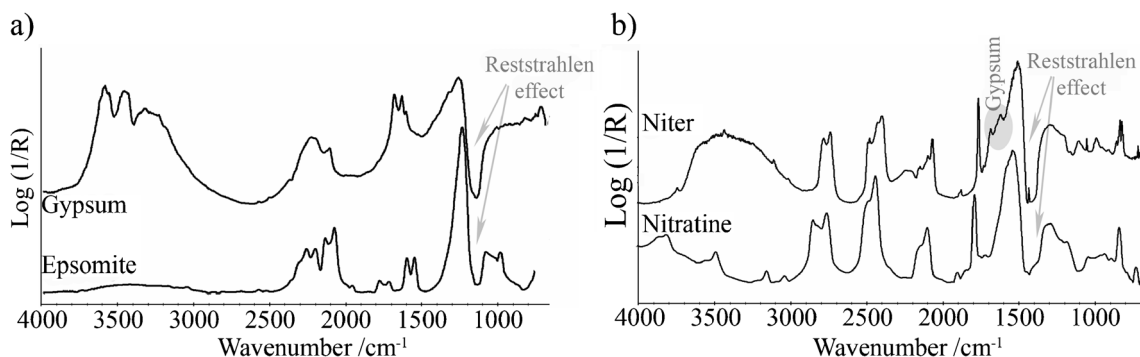

Fig. 3 DRIFT spectra of **a** gypsum identified in situ as a degradation compound of a black crust area, and **b** nitratine and niter collected in the sandstone ashlars in low-lying areas of the facade, next to a drainpipe

Table 2 Summary of material characterization done by nondestructive techniques

	Compounds indentified		
	DRIFT	Raman	XRD[b]
Silicates	Several silicates[a]	Quartz[a], kaolinite[a], muscovite[a], calcium silicate, albite	Quartz, phyllosilicates (kaolinite group, illite group)
Oxides	Hematite, goethite	Hematite[a], goethite[a], magnetite, limonite, lepidocrocite, rutile[a]	
Carbonates	Potassium carbonate[a], calcite[a]	Calcite[a]	
Sulfates	Gypsum[a], thenardite[a]	Anhydrite[a], gypsum[a], thenardite[a], epsomite[a], coquimbite	
Nitrates	Niter[a], nitromagnesite[a], nitratine[a]	Niter[a], nitromagnesite[a]	
Others		Carbon[a], salinixanthin	

DRIFT diffuse reflectance infrared Fourier transform, *XRD* X-ray diffraction

[a] Detected in situ

[b] Nondegraded sandstone samples

Finally, in areas with vegetation next to the drainpipe, calcite, gypsum, and nitrate were identified by their Raman bands at 1,085, 1,008, and 1,050 cm^{-1}, respectively. However, owing to the great fluorescence, it was not possible to discern which nitrate was present as this band is common to some of them. Nevertheless, the DRIFT analysis complemented the results, finding gypsum (assigned by the bands at 1,683 and 1,620 cm^{-1}), niter (KNO_3; identified by its bands at 2,736, 2,396, 2,066, 1,760, 1,490, and 825 cm^{-1}), and nitratine ($NaNO_3$; determined by its bands at 2,756, 2,435, 2,095, 1,786, 1,534, and 837 cm^{-1}) (Fig. 3b). These compounds could have originated by different mechanisms, although the most probable cause is the acid attack of the atmospheric NO_x gases on the feldspar cement of the stone, being aggravated by the penetration of water from the drainpipe. In fact, the growth of vegetation, observed only in this area, could be as a consequence of the water, and the roots of the vegetation could be promoting the infiltration of water into the material.

The inner side of the historical arch was studied in depth. According to the visual inspection, a great number of salt crusts were observed at different heights. Only one side of the arch shows this damage, its base being wet to the touch. Thus, the origin of the damage could be related to a problem of water infiltration, and therefore the spectroscopic study was done at different heights. Depending on the efflorescences found, the right side of the arch was divided into eight zones (Table 1) to determine the salt distribution model by spectroscopic techniques.

In this way, niter (identified by the presence of its whole Raman bands at 1,358, 1,344, 1,050, and 715 cm^{-1}) was found from the base (zones P1 and P2) of the arch up to a height of 1.6 m (zone P7). Besides, gypsum and calcite were determined mainly in the middle zone (zones P2 and P3). Above the middle level, thenardite (Na_2SO_4; identified by the strongest Raman peak at 991 cm^{-1} and the weakest pair of peaks at 466 and 451 cm^{-1} as well as by other signals at 1,149, 1,128,

644, 632, and 621 cm^{-1}) and epsomite ($MgSO_4 \cdot 7H_2O$; Raman band at 985 cm^{-1}) were identified, only over the joint mortars (zones P4 and P5). In zones P5 and P6, no salt crust was observed.

Afterward, DRIFT analysis of the same areas corroborated the existence of a special zoning salt distribution, which approximates the model of Arnold and Zehnder [44, 45]. In this way, the DRIFT spectra collected in zone P1 showed a mixture of two compounds. The signal obtained (Fig. 4a) was distorted in two regions, suggesting the presence of nitrate- and sulfate-containing compounds. Niter was identified as a major compound, although correct assignation of the sulfate was not possible owing to the Reststrahlen effect. In zone P2, gypsum and niter were found, but this time the major component was sulfate. Continuing with the DRIFT analysis by height, we detected a great amount of gypsum and some calcite in zone P3. However, only thenardite (identified by DRIFT bands at 2,180 and 2,104 cm^{-1}) was identified as a degradation compound in zone P4, with almost no sulfates being detected in the next zones (P5 and P6). Finally, in the upper level (zone P7), only niter was identified as a main compound of the salt crust, disappearing at the highest level, zone P8 (Fig. 4b).

According to the results, a progressive distribution of salts, whose origin seems to be the ingress of water from the subsoil, was observed [4]. In fact, the point of entry could be the base of the arch, since a large amount of sulfates and nitrates was detected at ground level (zone P1). The infiltration of groundwater and its rise by capillarity through the wall could cause severe damage. In this case, the loss of material observed could be a direct consequence of the physical stress suffered during hydration–dehydration processes as well as by transformation of original materials caused by dissolution–precipitation and crystallization processes. Clear examples of the water effect are the hydrolysis of feldspar cements and the equilibrium of thenardite with its decahydrated form, one of
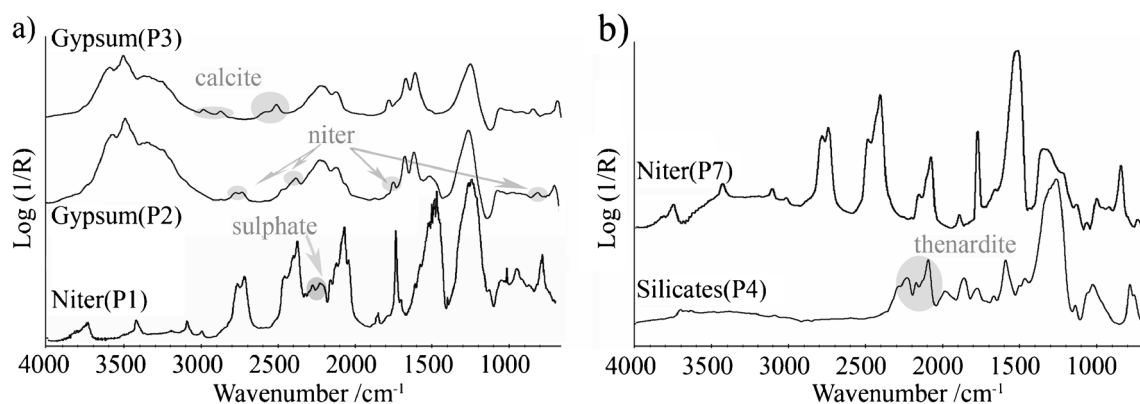
Fig. 4 DRIFT spectra collected in the arch of the inner wall: **a** niter, gypsum, and calcite found in zones P1, P2, and P3; **b** silicates, thenardite, and niter detected in zones P4 and P7

the salts most dangerous to building materials [4]. From all of this, and taking into account also the structural function of the wall, we suggest dangerous cracks could appear if no restoration is performed.

Laboratory results

X-ray diffraction

To increase the information on the original materials, two samples of nondegraded sandstones were analyzed. Quartz was the major compound, with an estimated proportion of 88 %. Besides, the remaining argillaceous content was identified as phyllosilicates of the kaolinite and illite groups (Table 2). Therefore, the main kind of sandstone could be classified as subarkose of micaceous cement, as the in situ analysis seemed to indicate.

DRIFT and Raman spectroscopy

According to the composition of the sandstone, several compounds were identified (Table 2). In this way, the presence of calcite, hematite (501 and 453 cm^{-1}), and silicates was corroborated as the *original composition* using the DRIFT laboratory equipment.

However, no distortions were observed in the spectra, since in the configuration of the laboratory equipment, the interference of specular reflection is almost eliminated. In addition, to reduce the specular component, the samples were ground (particles smaller than 10 μm), favoring the diffuse component of the sample surface. However, if the analyzed sample is highly absorbent, it can be diluted in a nonabsorbent matrix (KBr) to generate an even less specular component in the surface, increasing the contribution of the diffuse reflectance component. With these two simple operations, the specular component is reduced, achieving almost pure diffuse reflection spectra. An example is displayed in Fig. 5a, where the DRIFT spectrum of calcite recorded in situ with the handheld device and that

obtained in the laboratory can be compared, and it can be seen that the contribution of the specular reflection is nearly negligible. Therefore, the less intense bands have increased in intensity and, what is even more important, the spectra obtained in the laboratory are not distorted by the Reststrahlen effect.

On the other hand, Raman analysis complemented the in situ study, giving the full spectra of calcite, quartz, hematite, rutile, and kaolinite (Raman bands at 915, 795, 745, 460, 431, 333, 264, and 240 cm^{-1}). In addition, limonite [FeO(OH) · nH$_2$O; identified by its bands at 552, 394, 297, and 240 cm^{-1}], calcium silicate (Ca$_3$SiO$_5$; detected by its main bands at 1,075, 578, and 370 cm^{-1}), and albite (NaAlSi$_3$O$_8$; identified by its main bands at 507 and 478 cm^{-1}) were also found (Fig. 5b).

Regarding the original mortar composition, calcite, quartz and hematite were corroborated as major original compounds by Raman and DRIFT analysis.

The laboratory results for the reddish areas of the facade confirmed the results obtained in situ. Thanks to Raman spectroscopy, the presence of magnetite and goethite was confirmed. Besides, DRIFT analysis corroborated these results, detecting also goethite (by its characteristic infrared absorption bands at 3,129, 910, 798, and 623 cm^{-1}). Moreover, lepidocrocite (detected by its main Raman band at 250 cm^{-1}) was found. The presence of this intermediate transformation product evidenced that the degradation of ferruginous cement was occurring. In addition, the physical stress produced by the dissolution and crystallization of iron oxides, which leads to the bad state of conservation observed in these ashlars, was explained.

The analysis of the efflorescences collected in reddish areas revealed the presence of coquimbite [Fe$_2$(SO$_4$)$_3$ · 9H$_2$O); identified by its main Raman band at 1,025 cm^{-1}], gypsum, and some type of carbonate salt, maybe siderite (FeCO$_3$; Raman bands detected at 1,090 and 302 cm^{-1}). Once again, these compounds suggest that Guevara Palace suffered an atmospheric attack, since CO$_2$ and SO$_2$ gases are deteriorating the iron compounds of the facade, and their respective salts could
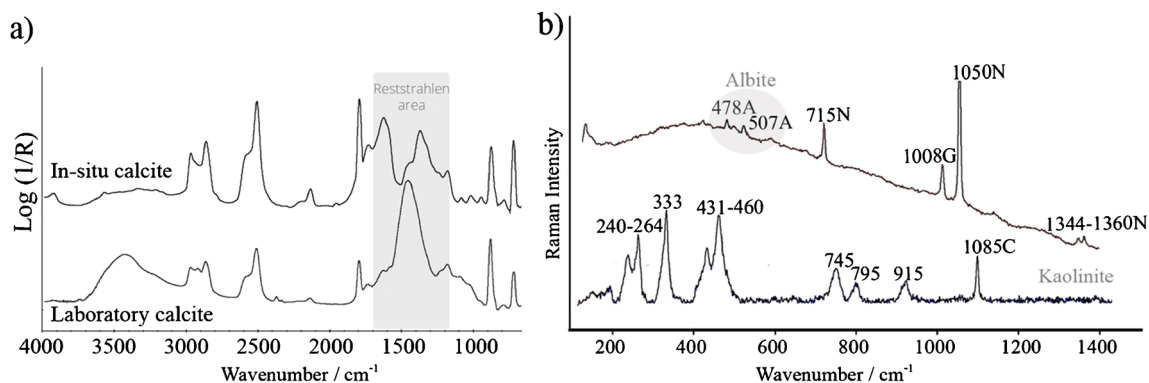
Fig. 5 **a** Comparison of the DRIFT spectrum of calcite collected in situ with the handheld device and the spectrum obtained in the laboratory. **b** Raman spectra collected in the laboratory. Kaolinite, calcite (*C*), gypsum (*G*), niter (*N*), and albite (*A*) were found in a facade sample of sandstone

be filtered to the stone, causing material loss by crystallization processes.

Finally, the results of in situ analyses of the areas with vegetation, close to the general drainpipe, were confirmed by both techniques, and in addition, the carotenoid salinixanthin (identified by Raman bands at 1,154, 1,512, and 1,003 cm^{-1}) was found. This unusual carotenoid is related to *Salinibacter*, which is normally present in red algae [46] and cannot grow below a salt concentration of 20 %. Thus, its detection together with the presence of algae in the stone could be used as a valuable indicator of salt weathering [47] when sampling is restricted.

Quantification of soluble salts by ion chromatography

To assess the salt distribution of the historical arch, the samples extracted at different heights (Table 1) were analyzed by ion chromatography. In this manner, soluble sulfate, nitrate, chloride, ammonium, sodium, potassium, calcium, and magnesium concentrations were quantified (Table 3).

The salts in the arch appear to be accumulated not only at the lower levels but also at higher levels as the in situ analyses indicated. Moreover, as is expected in the case of rising damp

[44, 48], distinct salt zones were observed depending on the height, suggesting the presence of infiltrated water from the ground level. Hence, the water was transporting and dissolving the salts from the inner part of the stone to the surface up to a height of 1.6 m.

The values from the ion chromatography analyses showed the presence of large quantities of sulfates up to zone P4 (0.6 m), with a decrease of concentration in zone P2 (0.2 m). Nitrates were also found from the lowest level to zone P7 (1.6 m) without showing high concentrations at intermediate points. However, chlorides seem to be more homogeneously distributed, suggesting their natural presence in the stone. In this way, the vertical distribution of salts was approximated to the model of Arnold and Zehnder [44, 45] as the less soluble sulfates such as gypsum, thenardite, and epsomite were accumulated in low and middle zones, whereas nitrates, mainly niter, were concentrated only in the lowest zone and at the top.

Given the salt distribution and the interruption of the concentration zones observed, the origin of the damage suffered by the historical arch is clearly caused by the capillary rise and evaporation of infiltration water. In this way, the leached content of the soil passed through the ashlars causing several instances of damage as a consequence of dissolution, hydration, and crystallization processes.

Low concentrations of sulfates at high points were determined, and therefore dragging of salts from plaster layers applied to the restoration was ruled out as the source of the damage. However, if the water infiltration is not stopped, dragging of salts will produce new problems, which may deteriorate even more rapidly the state of preservation.

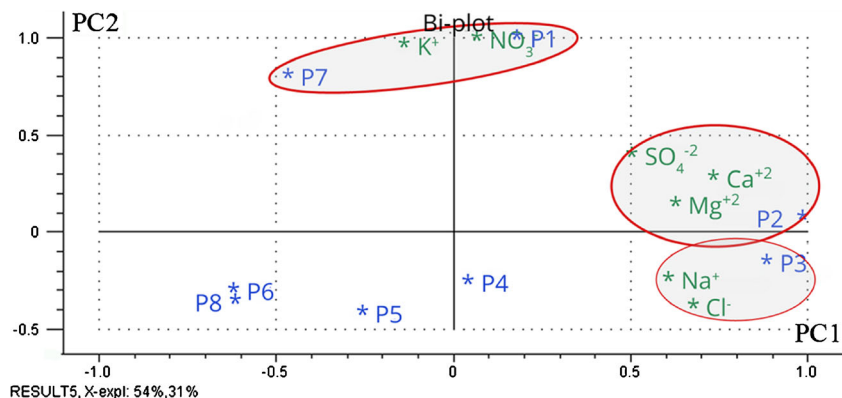*Principal component analysis of the ion chromatography results*

To corroborate if the vertical distribution of salts within the materials approximated what the spectroscopic results seem to indicate, a multivariate analysis of the data was performed to obtain further information on the correlation with ion chromatography analysis.

Table 3 Concentrations (mg cm^{-2}) and method repeatabilities (relative standard deviation, *RSD*) obtained by ion chromatography

Sample	Na$^+$	K$^+$	NH$_4^+$	Mg^{2+}	Ca^{2+}	Cl$^-$	NO$_3^-$	SO$_4^{2-}$
P1	0.02	2.19	<QL	0.02	0.26	0.01	5.89	0.51
P2	0.16	0.32	<QL	0.03	0.37	0.19	2.38	0.23
P3	0.14	0.15	<QL	0.02	0.32	0.27	1.65	0.37
P4	0.09	0.04	<DL	0.01	0.10	0.08	0.35	0.41
P5	0.05	0.05	<DL	0.01	0.00	0.13	0.46	0.08
P6	0.00	0.03	<DL	0.01	0.05	0.00	0.05	0.09
P7	0.01	2.70	<DL	0.01	0.00	0.01	3.80	0.04
P8	0.00	0.05	–	0.01	0.00	0.00	0.06	0.11
RSD (%)	2	6	–	2	4	3	4	4

DL limit of detection, *QL* limit of quantification

Fig. 6 Principal component analyses done by The Unscrambler. The graph shows the soluble content results obtained by ion chromatography. The groups formed according to principal component 1 (*PC1*) versus principal component 2 (*PC2*) are highlighted: nitrates, sulfates, and chlorides

The principal component analysis explained 89 % of the variance, using three principal components. As can be seen in Fig. 6, the grouping of three clusters is suggested: potassium and nitrate, calcium and magnesium sulfates, and sodium and chloride.

Sodium was most correlated with the chloride content ($r=$ 0.910), indicating their abundance in zone P3. However, as the quantitative results obtained by ion chromatography suggested, the presence of chlorides is natural in this kind of stone. However, they could be slightly more concentrated in this zone as a consequence of water ingress.

In the middle zone of the arch, sulfates of magnesium and calcium were correlated. This finding is supported by the identification of gypsum efflorescences by both spectroscopic techniques. Nevertheless, the in situ results for the surface showed the presence of thenardite and calcite also. Probably, the differences are caused by seasonal changes and/or the extraction method used, since these results correspond to a certain depth, and there may be differences in concentration between the exterior and interior zones.

Finally, potassium and nitrate were highly correlated ($r=$ 0.873), as the spectroscopic techniques identified niter as the main degradation compound in zones P1 and P7. Once again, capillary rise up the wall is suggested.

In this manner, the quantitative results and the chemometric study demonstrate the damage suffered by the ashlars is produced by the hydration–dehydration and dissolution–precipitation cycles. Moreover, the study complemented the in situ analysis, revealing the presence of chlorides as original compounds.

Thermodynamic modeling: degradation mechanisms of the cementitious matrix and iron salt formation

Given that the sandstone of ferruginous cement is a typical construction material of Basque built heritage, this thermodynamic study aimed to predict the formation of the identified degradation compounds to understand the mechanisms involved in its degradation, since the dissolution of the stone cement could cause severe disaggregations and material losses.

Ferruginous cement, mainly composed of hematite (α-Fe_2O_3), can be transformed to goethite (α-FeOOH) by intermediate mechanisms that occur in an aqueous medium as the Pourbaix diagram [49] indicates. Depending on the potential of the medium and the pH, hematite can release Fe^{2+} cations (Fig. 7a), which are hydrated first to generate the thermodynamically less stable species lepidocrocite (γ-FeOOH) [40].
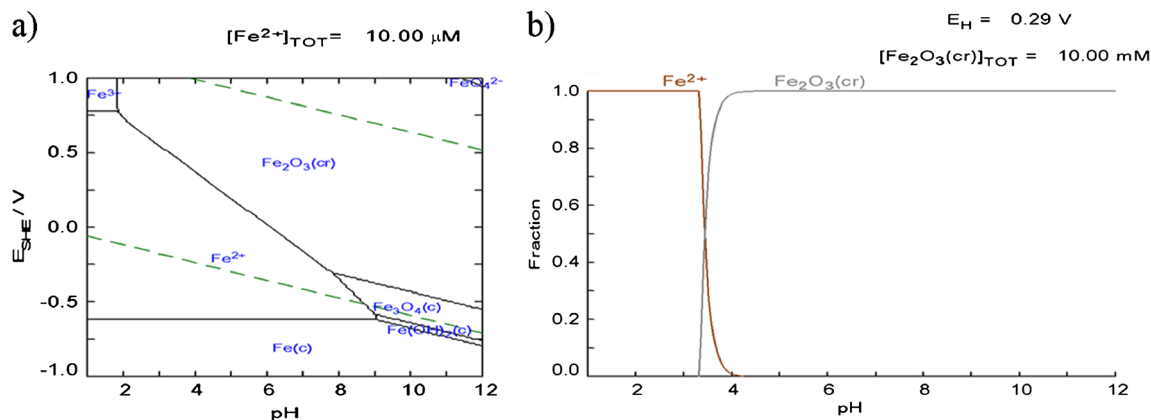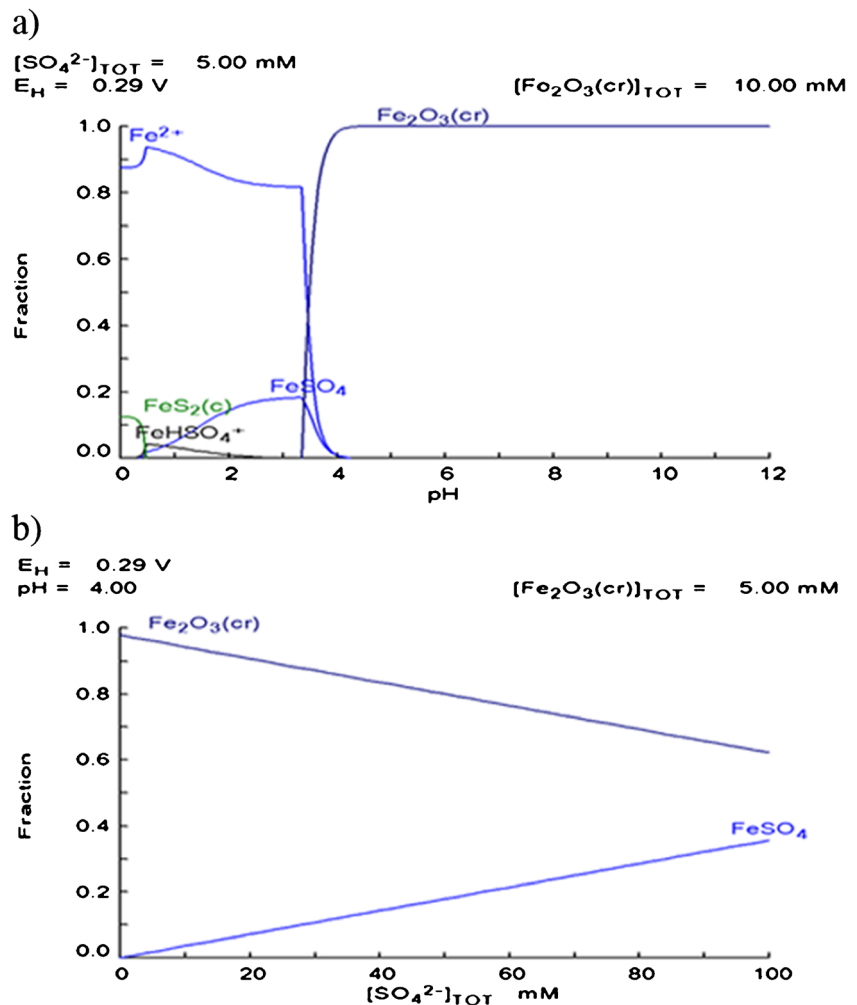

Fig. 7 a Pourbaix diagram with phase changes experienced by the different iron compounds as a function of pH and redox potential of the medium. **b** Molar fraction diagram of hematite depending on the pH of the medium

Fig. 8 Molar fraction diagram of iron sulfate formation depending on **a** pH and **b** concentration of sulfated pollutants

a)

$[SO_4^{2-}]_{TOT} = 5.00\ mM$
$E_H = 0.29\ V$
$[Fe_2O_3(cr)]_{TOT} = 10.00\ mM$

b)

$E_H = 0.29\ V$
$pH = 4.00$
$[Fe_2O_3(cr)]_{TOT} = 5.00\ mM$

The latter is transformed quickly into the stabler goethite. According to the results, these transformations were occurring, as the presence of lepidocrocite and goethite was detected.

Because the measured redox potential was about 0.29 V, the pH necessary for the release of Fe^{2+} cations had to be lower than 4.5 (Fig. 7b). This value can be easily achieved in the pores of the stone by the action of environmental pollutants and their deposition on materials.

The Raman spectrum of coquimbite—$Fe_2(SO_4)_3 \cdot 9H_2O$—proves again that the degradation suffered by the ferruginous cement is due to the action of CO_2 and SO_x gases. In this manner, in conditions that may occur in the porous network, the formation of iron sulfate (Fig. 8a) is predicted at pH values lower than 4.5. Then coquimbite is produced by a hydration process. At this point, its amount will depend on the concentration of pollutants in the environment (Fig. 8b).

All of these mechanisms have harmful consequences for materials since the behavior of stone against the stresses or strains can cause deformation and fractures, depending on the petrologic and petrographic properties (degree of cementation,

porosity type, etc.) and the external conditions in which the rock suffers tension (temperature, presence of water, etc.). Therefore, the mechanical strength that determines its durability could be seriously affected, resulting in serious damage.

To prevent and stop these deterioration phenomena, consolidant products can be used. In the absence of a cementitious matrix, they can fix the grains of the material, providing strength and more durability to ashlars. To ensure the reliability of the interventions, it is necessary to perform studies of this type to determine the suitability of the consolidant used, and in this way, select the most appropriate one for each case.

Conclusions

The multianalytical method performed allowed us to demonstrate that the main source of the decay process observed in the facade was the effect of atmospheric pollutants, also detecting damage promoted by biodeterioration in areas close to the main drainpipe. However, the poor state of preservation

observed in the historical arch was related to the infiltration of water and its capillary rise up the firewall.

Moreover, the advantages and usefulness of DRIFT spectroscopy as a useful tool in the identification of compounds and salt zoning distribution were highlighted, as this technique significantly minimizes the problems presented in Raman spectroscopy by the effect of fluorescence in samples of this kind, making the identification of a higher number of compounds possible and helping to interpret the Raman spectra obtained (e.g., it was indispensable for the identification of various silicates). Therefore, this work shows the complementarity of these nondestructive techniques in the field of built heritage.

Although in situ DRIFT analyses are affected by external factors, if the procedures are followed correctly, minimization of the effects is possible and good in situ spectra can be obtained if the sample interface makes stable contact with the sample surface. However, the diffuse reflectance interface fits better with not too hard samples, allowing better contact and achieving a good spectrum in a single measurement, instead of with hard samples, in which the contact is not complete and several measurements are needed to obtain a good spectrum. Iron oxides cannot be observed by means of in situ DRIFT analysis as the main vibration signals appear around 900 cm^{-1}, which is the same area that is distorted by the Reststrahlen effect. However, to achieve good laboratory results, simple operations such as grinding and mixing the sample with a nonabsorbent compound can minimize the contribution of the specular component successfully to determine them.

In addition, the usefulness of DRIFT spectroscopy in the field could be improved if existing databases included more standards, thus allowing the identification of the silicates and organic signals collected in the in situ analysis.

Finally, given the differences observed in the results caused by seasonal changes, monitoring of the salts present is advised in order to select the most suitable resin or inhibitor to prevent the progress of existing damage to the arch.

References

1. Appolonia L, Vaudan D, Chatel V, Aceto M, Mirti P (2009) Anal Bioanal Chem 391:2005–2013
2. Vandenabeele P, Castro K, Hargreaves M, Moens L, Madariaga JM, Edwards HGM (2006) Anal Chim Acta 588:108–116
3. Medina J, Rull F, Sanz A, Sanz C, Gazquez F (2013) Macla 17:73–74
4. Gómez-Laserna O, Olazabal MA, Morillas H, Prieto-Taboada N, Martinez-Arkarazo I, Arana G, Madariaga JM (2013) J Raman Spectrosc 44:1277–1284
5. Andrikopoulos KS, Daniilia S, Roussel B, Janssens K (2006) J Raman Spectrosc 37:1026–1034
6. Aramendia J, Gomez-Nubla L, Castro K, Martinez-Arkarazo I, Vega D, Sanz López de Heredia A, García Ibáñez de Opakua A, Madariaga JM (2012) J Raman Spectrosc 43:1111–1117
7. Julleh M, Alalur J, Ahman R, Higeyuki S, Uzuki S (2007) Geochem J 41:415–428
8. Arostegui J, Irabien MJ, Nieto F, Sangüesa J, Zuluaga MC (2001) Clays Clay Miner 49:529–539
9. Prieto-Taboada N, Ibarrondo I, Gómez-Laserna O, Martínez-Arkarazo I, Olazabal MA, Madariaga JM (2013) J Hazard Mater 249:451–460
10. Jehlička J, Vítek P, Edwards HGM, Hargreaves M, Čapoun T (2009) J Raman Spectrosc 40:1645–1651
11. Kavkler K, Gunde-Cimerman N, Zalar P, Demsar A (2011) Polym Degrad Stab 96:574–580
12. Navas N, Romero-Pastor J, Manzano E, Cardell C (2008) Anal Chim Acta 630:141–149
13. Vetter W, Schreiner M (2011) e-Preserv Sci 8:10–22
14. Chércoles Asensio R, San Andrés Moya M, De la Roja JM, Gómez M (2009) Anal Bioanal Chem 395:2081–2096
15. Genestar C, Pons C (2005) Anal Bioanal Chem 382:269–274
16. Bicchieri M, Monti M, Piantanida G, Pinzari F, Sodo A (2011) Vib Spectrosc 55:267–272
17. Prati S, Rosi F, Sciutto G, Mazzeo R, Magrini D, Sotiropoulou S, Van Bos M (2012) Microchem J 103:79–89
18. Anselmi C, Presciutti F, Doherty B, Brunetti BG, Sgamellotti A, Miliani C (2011) Appl Phys 104:401–406
19. Ricci C, Miliani C, Brunetti BG, Sgamellotti A (2006) Talanta 69:1221–1226
20. Poli T, Elia A, Chiantore O (2009) e-Preserv Sci 6:174–179
21. Miliani C, Rosi F, Daveri F, Brunetti BG (2012) Appl Phys A 106:295–307
22. Arrizabalaga I, Gomez-Laserna O, Aramendia J, Arana G, Madariaga JM (2014) Spectrochim Acta A 129:259–267
23. Kortum G (1969) Reflection spectroscopy. Springer, Berlin
24. Arrizabalaga I, Gomez-Laserna O, Aramendia J, Arana G, Madariaga JM (2014) Spectrochim Acta A 124:308–314
25. Goudie AS, Viles HA (1997) Salt weathering hazards. Wiley, Chichester
26. Prieto-Taboada N, Isca C, Martínez-Arkarazo I, Casoli A, Olazabal MA, Arana G, Madariaga JM (2014) Environ Sci Pollut Res 21:12518–12529
27. Dionísio A, Martinho E, Grangeia C, Almeida F (2012) Switzerland global stone congress. Trans Tech Publications, Pfaffikon, pp 170–177
28. E.V.E (2010) Mapa geológico del País Vasco. E.V.E, Beasain
29. Basque Government (2014) Agencia Vasca del agua, Seguimiento de ríos y Medioambiente. http://www.uragentzia.euskadi.eus/u81-0002/es/
30. Arnold A, Zehnder K (1991) In: Cather S (ed) The conservation of wall paintings. The Getty Conservation Institute, Los Angeles, pp 103–135
31. Castro K, Perez-Alonso M, Rodriguez-Laso MD, Fernández LA, Madariaga JM (2005) Anal Bioanal Chem 382:248–258
32. Pérez-Alonso M, Castro K, Madariaga JM (2006) Anal Chim Acta 571:121–128
33. Maguregui M, Prieto-Taboada N, Trebolazabala J, Goienaga N, Arrieta N, Aramendia J, Gomez-Nubla L, Sarmiento A, Olivares M, Carrero JA, Martinez-Arkarazo I, Castro K, Arana G, Olazabal

MA, Fernandez LA, Madariaga JM (2010) Congress of Chemistry for Cultural Heritage (ChemCH). pp 168–170

34. Downs RT (2006) IMA 19th general meeting of the international mineralogical association in Kobe, Japan, p 117

35. Prieto-Taboada N, Gómez-Laserna O, Martinez-Arkarazo I, Olazabal MA, Madariaga JM (2012) Ultrason Sonochem 19: 1260–1265

36. Puigdomenech I, Zagorodni A, Wang M, Muhammed M (2009) Program Medusa (make equilibrium diagrams using sophisticated algorithms). Royal Institute of Technology, Inorganic Materials Chemistry, Sweden

37. Bathurst RGC (1975) Carbonate sediments and their diagenesis. Developments in sedimentology. Elsevier, Amsterdam

38. Fregenal M, López Gómez J, Martín Chivelet J (2000) Ciencias de la Tierra. Diccionarios Oxford-Complutense. Complutense, Madrid

39. Korte EH, Roseler A (2005) Anal Bioanal Chem 382:1987–1992

40. Cornell RM, Schwertmann U (2003) The iron oxides: structure, properties, reactions, occurrences and uses. Wiley, Weinheim

41. Scwhertmann U, Taylor RM (1972) Clay Clay Miner 20:151–158

42. Manning M (1988) Air pollution, acid rain and the environment: corrosion of building materials due to atmospheric pollution the United Kingdom. Springer, Dordrecht

43. Bai Y, Thompson GE, Martinez-Ramirez S, Brüeggerhoff S (2003) Sci Total Environ 302:247–251

44. Agudo ER, Lubelli B, Sawdy A, Hees RV, Price C, Navarro CR (2011) J Environ Earth Sci 63:1475–1486

45. Vázquez MA, Galán E, Ortiz P, Ortiz R (2013) J Constr Build Mater 45:95–105

46. Jehlička J, Osterrothová K, Nedbalová L, Gunde-Cimerman N, Oren A (2014) 11th International GeoRaman Conference. p 5042

47. Oren A (2013) Microbiol Lett 342:1–9

48. Siegesmund S, Snethlage R (2011) Stone in architecture: properties, durability. Spinger, Heidelberg

49. Pourbaix M (1974) Atlas of electrochemical equilibria in aqueous solutions. National Association of Corrosion Engineers, Houston